Check for updates

Advanced Energy Materials

ADVANCED ENERGY MATERIALS
www.advenergymat.de

RESEARCH ARTICLE OPEN ACCESS

Chemical Rounding Suppresses Morphology-Induced Interfacial Losses in Perovskite–Silicon Tandem Solar Cells

Nan Sun[1,2] | Binbin Xu[1,3] | Gaosheng Huang[1,3] | Yuehui Li[4] | Karsten Bittkau[1] | Eunseo Noh[5] | Sercan Aslan[1,3] | Andreas Lambertz[1] | Sang Il Seok[5] | Michael Saliba[1,6] | Christoph J. Brabec[1,7] | Thomas Kirchartz[1,2] | Kaining Ding[1,3]

[1]IMD-3 Photovoltaics, Forschungszentrum Jülich GmbH, Jülich, Germany | [2]Faculty of Engineering and CENIDE, University of Duisburg-Essen, Duisburg, Germany | [3]Jülich Aachen Research Alliance (JARA-Energy) and Faculty of Electrical Engineering and Information Technology, RWTH Aachen University, Aachen, Germany | [4]Institute of Quantum Materials and Physics, Henan Academy of Sciences, Zhengzhou, China | [5]Department of Energy and Chemical Engineering, Ulsan National Institute of Science and Technology (UNIST), Ulsan, South Korea | [6]Institute For Photovoltaics (Ipv), Research Center SCoPE, and Integrated Quantum Science and Technology Center (IQST), University of Stuttgart, Stuttgart, Germany | [7]Institute of Materials for Electronics and Energy Technology (i-MEET), Friedrich-Alexander University Erlangen-Nürnberg, Erlangen, Germany

Correspondence: Nan Sun (n.sun@fz-juelich.de) | Michael Saliba (michael.saliba@ipv.uni-stuttgart.de) | Thomas Kirchartz (t.kirchartz@fz-juelich.de) | Kaining Ding (k.ding@fz-juelich.de)

Received: 24 June 2026 | **Revised:** 19 October 2026 | **Accepted:** 26 October 2026

Keywords: amorphous silicon | crystalline silicon | epitaxy | micro texture | perovskite | tandem

ABSTRACT

Surface texturing in crystalline silicon solar cells imposes a fundamental trade-off in perovskite-silicon tandems: micrometer-scale pyramids enable efficient light trapping but limit the conformal deposition of thin perovskite films with sub-micrometer thickness, whereas reduced texture heights improve compatibility at the expense of optical performance and interfacial quality of the tandem device. Here, we address this challenge by combining precisely controlled submicron texturing with an ozone-assisted chemical rounding treatment. The resulting silicon substrates feature smoothly rounded, symmetric submicron textures that suppress micro-terrace formation and partial epitaxy at the amorphous silicon/crystalline silicon interface, while promoting more spatially uniform optoelectronic properties in the subsequently integrated top-cell stack. The morphology-engineered texture yields a monolithic perovskite–silicon tandem device with a power conversion efficiency of 33.25%, demonstrating that multiscale morphological control provides a powerful pathway to simultaneously improve the optical performance and interfacial quality of tandem solar cells.

1 | Introduction

Monolithic perovskite–silicon tandem (PST) solar cells have emerged as one of the most promising architectures for surpassing the efficiency limit of single-junction solar cells. For silicon, the current certified single-junction record is 26.8%, which approaches the theoretical limit of 29.4% imposed by intrinsic Auger recombination [1–3]. A recent report demonstrated efficiencies beyond 35% in certified monolithic tandem solar cells [4], highlighting the rapid progress in device performance. Among various tandem configurations, silicon heterojunction (SHJ) bottom cells [5–7] are particularly attractive owing to their high open-circuit voltage, low-temperature manufacturing compatibility, and well-established texturing techniques that facilitate optical trapping [8–10].

However, the surface texture that enhances optical absorption poses persistent challenges for the subsequent deposition of wide-bandgap perovskite (PVSK) absorbers onto these surfaces. Conventional micron-scale textures used in industrial SHJ

This is an open access article under the terms of the Creative Commons Attribution License, which permits use, distribution and reproduction in any medium, provided the original work is properly cited.
© 2026 The Author(s). *Advanced Energy Materials* published by Wiley-VCH GmbH

cells require complex evaporation-based perovskite processing to ensure adequate conformal coverage of the textured surfaces. Submicron-scale pyramids are inherently more compatible with solution-processed perovskites but come at the expense of reduced infrared light scattering unless the morphology is carefully engineered. This trade-off between light management and film conformality renders the buried silicon texture morphology a critical but still underexplored design parameter for PST integration.

Here, we identify and realize a morphology-governed pathway that reconciles these competing optical and interfacial requirements. Guided by optical simulations, we determine the submicron texture height and morphology that maximize photon utilization while maintaining uniform perovskite coverage. However, translating this design into practice introduces a new challenge unique to submicron textures. Compared to micron-textures, shallow alkaline etching inherently produces nanoscale irregularities and micro-terraces that act as preferential templates for partial epitaxy at the hydrogenated amorphous silicon/crystalline silicon (a-Si:H/c-Si) interface. These defective ordered domains compromise the passivation quality and limit the carrier lifetime, presenting a morphology-induced interfacial bottleneck. Previous studies have also shown that chemical polishing of submicron silicon textures can improve surface morphology and passivation [11–13]. However, the microscopic origin of this passivation improvement, particularly the role of local surface irregularities in a-Si:H growth at the c-Si interface, remains insufficiently resolved. Here, we apply an ozone (O_3)-assisted chemical rounding strategy to smooth the step-rich features without sacrificing optical performance and directly examine the resulting a-Si:H/c-Si interface using atomic-resolution scanning transmission electron microscopy (STEM). The rounded textures exhibit reduced interfacial irregularities and suppressed partial epitaxial ordering, consistent with improved interface passivation, while providing a more regular morphological template for subsequent top cell integration.

These findings identify the morphology of textured silicon as a critical interfacial factor in PST integration and motivate further engineering of the buried texture morphology. The resulting rounded symmetric texture significantly improves the interface quality and, consequently, enables high-performance monolithic tandem devices, achieving an efficiency of 33.25% on a 1.014 cm^2 cell. These results establish that multiscale morphological control provides a powerful pathway to simultaneously optimize optical performance and interfacial quality in tandem solar cells.

1.1 | Optical Simulation on Tandem Device From Bottom-Cell Architecture Perspective

To guide the practical design rules for the morphology of buried silicon, we performed optical simulations of a monolithic tandem architecture featuring a solution-processed perovskite top cell (Figure 1a). The key structural parameters used in the simulations are summarized in Table S1. Six representative surface morphologies [7, 14–16] (Figure 1b), combining planar, single-side, and double-side textures, were constructed to evaluate how the light-trapping strength varies across texture designs. The effective pathlength enhancement factor k_{eff} [17] was introduced to quantify how surface geometry governs light scattering capability. The PVSK absorber is marginally affected by morphology due to its intrinsically strong absorption [18], while Si subcell benefits substantially (Figure 1c). Single-side texture raises k_{eff} from 2.1 to $\sim$ 6, and symmetric textures push it above 7 due to combined effects of front-side diffraction and rear-side reflection [17]. Detailed absorption, reflection and parasitic loss analyses are provided in Table S2 and Figures S3 and S4. The methodological details are provided in our previous work [19]. Given the minor optical gain but higher fabrication complexity of asymmetric designs, we focused on a symmetric configuration for subsequent simulations and experiments.

We subsequently varied the pyramid height (h) and Si wafer thickness to evaluate their impact under a constant PVSK-volume condition consistent with solution coating. Increasing h from 200 to 1100 nm enhances the infrared absorption in the Si subcell (Figure 1d); however, the gain levels off at $h > 500$ nm once multiple internal reflections are fully established. At even larger values of h, the net optical benefit diminishes because solution coating yields compromised PVSK coverage on high-aspect-ratio textures. Two limiting coating scenarios were additionally considered, mimicking perovskite underfilling and overfilling of the texture (Table S3 and Figure S5). These simulations confirm that a moderate submicron texture height provides the optimal balance between light trapping and realistic film uniformity, as shown in Figure S6.

Finally, we varied the Si wafer thickness from 80 to 280 µm, covering the range commonly used in laboratory and industrial applications [20–22]. The PVSK photocurrent remains essentially independent of the Si thickness (Figure S7), whereas current matching requires the PVSK thickness to scale with the wafer thickness (Figure 1e). Together, these simulations define a practical morphology window: a symmetric submicron texture featuring moderate pyramid height combined with a realistic wafer thickness. This window provides an optical design target for the submicron texture construction and rounding discussed below. A detailed analysis of the best case for absorption and optical losses in each layer is presented in Figure S8.

1.2 | Submicron Texture Construction and Morphology Modification

Figure 2a summarizes the simulated photocurrent of the Si bottom cell (J_{Si}) as a function of the pyramid height. The flat, untextured Si surface yields J_{Si} of 18.9 mA cm^{-2}. After texturing, dense and homogeneous pyramid arrays formed on the Si wafer, facilitating a significant increase in J_{Si} above 20 mA cm^{-2}. Guided by optical analysis, we translated the simulated design into experimentally controllable submicron textures that enable precise adjustment of the pyramid height and surface morphology. The objectives were twofold: (i) to realize reproducible submicron textures that preserve the optical benefits, and (ii) to refine the surface at the atomic scale for high-quality heterointerfaces.

Compared with conventional micron-scale texturing, achieving a uniform submicron texture is fundamentally more challenging [23, 24], because the shallow etching regime makes it difficult to balance facet nucleation and growth [25]. To address this

16146840, 0, Downloaded from https://advanced.onlinelibrary.wiley.com/doi/10.1002/aenm.71784 by Universitatsbibliothek RWTH Aachen University, Wiley Online Library on [13/11/2025]. See the Terms and Conditions (https://onlinelibrary.wiley.com/terms-and-conditions) on Wiley Online Library for rules of use; OA articles are governed by the applicable Creative Commons License

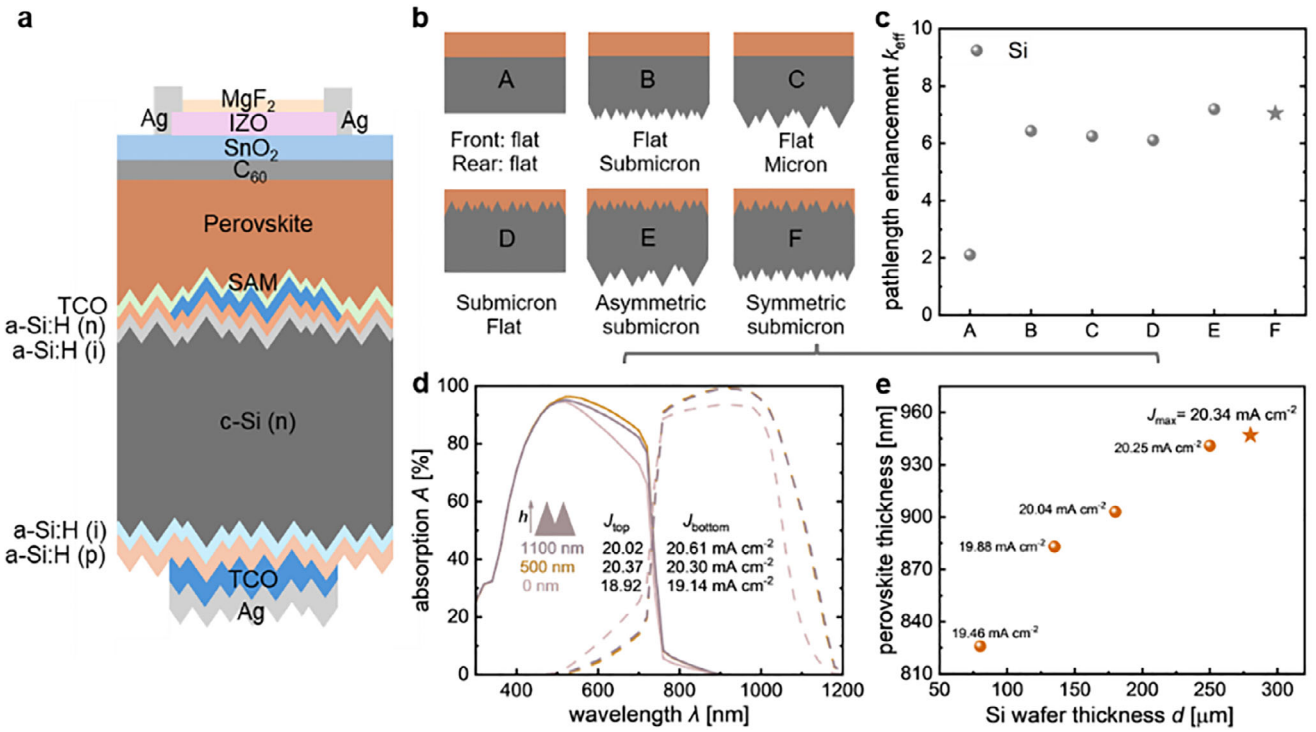

FIGURE 1 | (a) Schematic of the tandem device structure used in the simulations. (b) Sketch of the six different surface morphology types for the Si substrate. (c) Pathlength enhancement coefficient k_{eff} of Si absorbers with different morphological structures. (d) Absorption of top and bottom cells with varied pyramid heights. (e) Matched current densities for varying Si wafer and PVSK thicknesses.

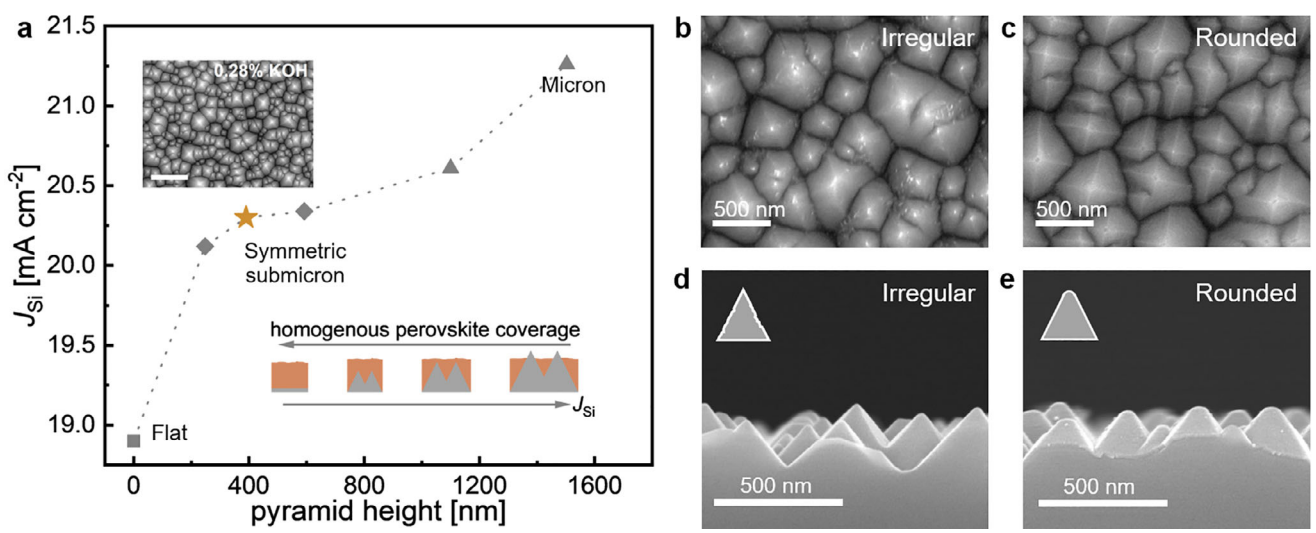

FIGURE 2 | (a) The photocurrent of the Si subcell is shown as a function of pyramid height. The inset shows the SEM image of the optimum-height submicron texture. Top-view SEM images of (b) irregular and (c) rounded Si substrates. Cross-sectional SEM images of (d) irregular and (e) rounded Si bottom cells.

limitation, we developed a simple solution-processed approach to achieve controllable submicron texture through adjusting the concentration of potassium hydroxide (n_{KOH}) in texturing solution. In contrast to the fabrication of micron-sized textures, submicron texture fabrication requires slower etching in the reaction-limited regime. The reduced OH^- concentration suppresses anisotropic etching and limits facet formation, thereby producing a submicron texture. The scanning electron microscopy (SEM) images of the texture and the histogram of the height distribution are shown in Figure S9.

Limiting n_{KOH} at 0.23% yielded compact pyramids with an average height of 248 nm and a narrow height distribution. Such shallow features ensure better surface coverage for the perovskite top layer

16146840, 0, Downloaded from https://advanced.onlinelibrary.wiley.com/doi/10.1002/aenm.71784 by Universitatsbibliothek RWTH Aachen University, Wiley Online Library on [13/11/2025]. See the Terms and Conditions (https://onlinelibrary.wiley.com/terms-and-conditions) on Wiley Online Library for rules of use; OA articles are governed by the applicable Creative Commons License

but provide limited light scattering in the infrared region [26]. Increasing n_{KOH} to 0.28% accelerated etching, promoting (111) facet development and increasing the mean pyramid height to 363 nm, which is close to the simulated optimum for balancing optical management and perovskite coverage. Further increasing n_{KOH} to 0.33% produces larger pyramids but also broadens the height distribution, enhancing light trapping in the Si subcell while increasing the risk of incomplete perovskite coverage and electrical shunting in the final tandem device [23]. This observation indicates that the average height alone is not an adequate criterion for assessing the suitability of submicron textures for PST. Instead, both the mean pyramid height and its statistical distribution must be carefully controlled during texturing to ensure reliable perovskite deposition and stable tandem integration. Figure 2a highlights the height window required to simultaneously maximize optical absorption and ensure perovskite coverage. As shown additionally, the micron-sized texture further improved J_{Si} over 21 mA cm^{-2} at the expense of perovskite coverage. The corresponding reflectance spectra are shown in Figure S10.

However, the slow kinetics that enable fine height control also introduce a new challenge: irregularities and micro-terrace formation are intrinsically more pronounced in submicron textures than in micron-textures. Because the etching depth is shallow, the (111) facets do not fully develop, and even subtle local variations in the OH^- supply, surface energy, or residual polishing damage can directly manifest as nanoscale morphological irregularities [12, 27]. These irregularities include facet truncation, shallow depressions, and low-angle micro-terraces (Figure 2b). Given the sub-micron characteristic length scale, even sub-nanometer variations in the local etch depth can create locally flattened regions with extremely small miscut angles. Such micro-terraces are rarely detectable on conventional pyramids with large and highly stable facets, but they become structurally dominant in submicron textures. Importantly, these micro-terraces act as atomically favorable templates for plasma-enhanced chemical vapor deposition (PECVD)-induced ordering, making submicron textures markedly more susceptible to partial epitaxy at the a-Si:H/c-Si interface.

To mitigate these morphology-induced defects, we introduced an O_3-assisted chemical rounding process, which smoothens step-rich features without compromising optical performance. Chemical smoothing or rounding of textured Si surfaces has previously been investigated as an approach to reduce sharp morphological features and improve surface passivation in SHJ solar cells [13, 28]. The process proceeds through sequential oxidation and isotropic oxide removal [29] described by the two reactions

$$Si + 2O_3 \rightarrow SiO_2 + 2O_2 \quad (1)$$

$$SiO_2 + 6HF \rightarrow H_2SiF_6 + 2H_2O \quad (2)$$

In this reaction scheme, O_3 first oxidizes the exposed Si surface to form a thin SiO_2 layer, which is subsequently dissolved by hydrofluoric acid (HF). Because oxide formation and dissolution occur preferentially at protruding regions such as pyramid tips and step-bunched facets, the overall texture evolves toward rounded, symmetric pyramids with well-defined, cleaner (111) facets (Figure 2c,e). Wide-angle cross-sectional SEM images further confirm that chemical rounding preserves the overall submicron pyramid geometry while primarily modifying local curvature and step-rich surface features (Figure S11). Notably, the cross-sectional SEM images in Figure 2d,e were acquired after ITO deposition. The characteristic differences between the irregular and rounded textures therefore remain distinguishable after TCO coating. The improved regularity not only facilitates conformal layer deposition in subsequent steps but also reduces the local field concentration at sharp features [14], both of which are beneficial for passivation and carrier transport in the bottom cell. As expected from their reduced angular sharpness, the rounded textures slightly increased the reflectance of the substrate (Figure S12), which is consistent with weaker forward scattering [29].

1.3 | Passivation of SHJ Bottom Cell

It is well known that a-Si:H films deposited by PECVD are highly sensitive to the microscopic structure of the underlying surface [30, 31]. To probe the impact of pyramid geometry on the structural quality of the heterointerface, atomic-resolution STEM was performed to characterize the ITO/a-Si:H/c-Si cross-section. As depicted in Figure 3a,b, the dashed orange lines mark the interfaces between layers.

In the irregular textured sample (Figure 3a), the lattice fringes extend continuously from the c-Si substrate into the a-Si:H layer, indicating epitaxial crystalline formation at the interface. This behavior is attributed to the roughened (111) facets of the pyramids formed during alkaline texturing, where step edges, kinks and local wrinkles act as atomic templates that promote local ordering during PECVD growth. Consistently, the corresponding fast Fourier transform (FFT) patterns extracted from regions 1 and 2 exhibit distinct crystalline diffraction spots, confirming the partial alignment of the amorphous film with the underlying c-Si lattice. Such epitaxial features can introduce structural defects within the transition zone and thereby deteriorate interface passivation. Taken together, these observations associate local nanoscale surface irregularities with partial epitaxial ordering at the a-Si:H/c-Si interface.

By contrast, the rounded configuration (Figure 3b) yields a well-defined, fully amorphous a-Si:H interlayer, as evidenced by the diffuse FFT halos in regions 3 and 4. The smooth, symmetric (111) facets produced by chemical rounding facilitate more conformal PECVD growth and effectively suppress local ordering, yielding a structurally abrupt a-Si:H/c-Si interface with a reduced density of structural defects. Additional FFT patterns from different interfacial zones are summarized in Figure S13. Figure 3c schematically illustrates the morphology-governed growth mechanism, highlighting the suppression of epitaxial nucleation on rounded facets in favor of homogeneous amorphous growth. The improved interfacial structure directly translates into enhanced passivation quality, as reflected in the statistical electrical metrics measured on bottom-cell precursors. As shown in Figure 3d, the rounded samples show markedly higher minority carrier lifetimes, signifying enhanced chemical passivation and reduced density of interfacial defects. These results confirm that atomic-scale morphological

16146840, 0, Downloaded from https://advanced.onlinelibrary.wiley.com/doi/10.1002/aenm.71784 by Universitatsbibliothek RWTH Aachen University, Wiley Online Library on [13/11/2025]. See the Terms and Conditions (https://onlinelibrary.wiley.com/terms-and-conditions) on Wiley Online Library for rules of use; OA articles are governed by the applicable Creative Commons License

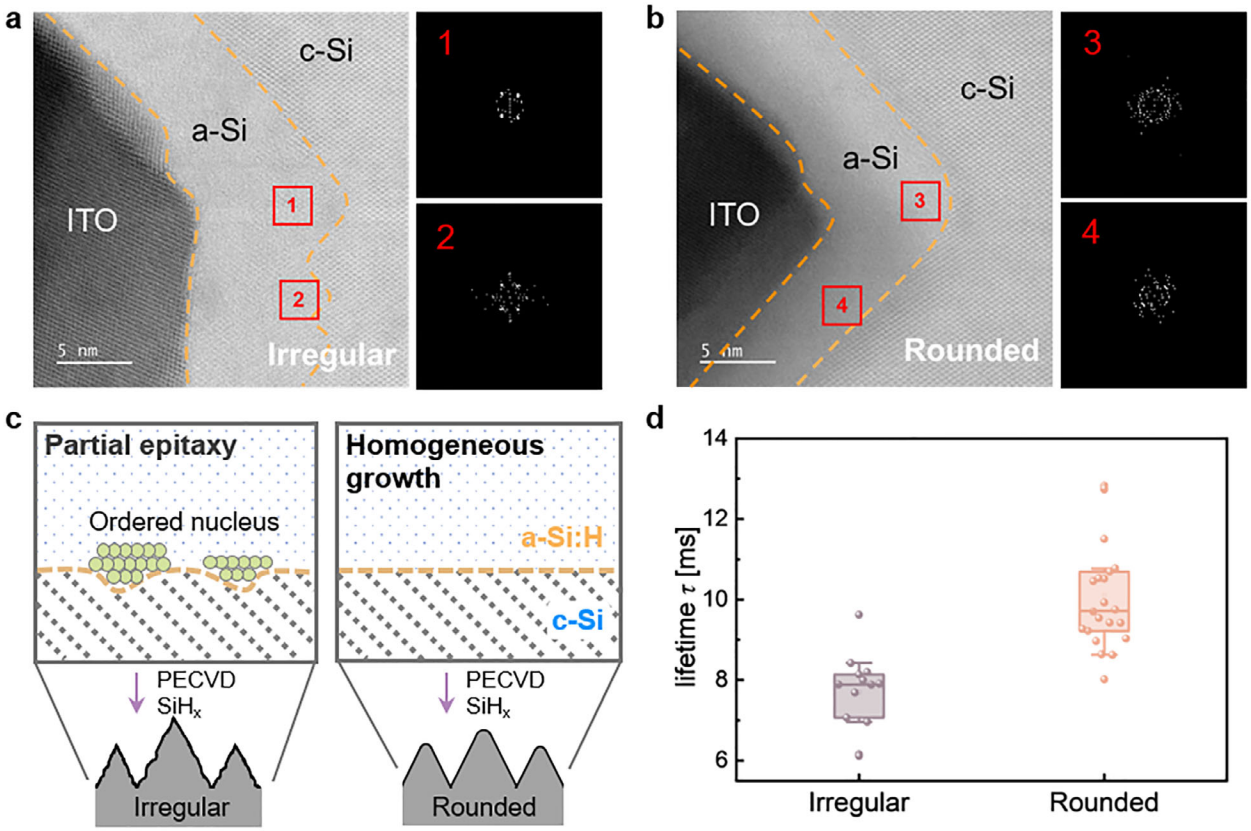

FIGURE 3 | Cross-sectional atomic-resolution STEM images of (a) irregular textured and (b) rounded textured bottom cells. The dashed yellow lines indicate the interfaces, and the diffraction patterns of the red window areas are shown in the adjacent panels. (c) Schematic illustration of the morphology-dependent growth mechanism during PECVD. (d) Effective minority carrier lifetimes (at $\Delta n = 5 \times 10^{15}$ cm^{-3}) of irregular textured and rounded textured bottom cell precursors.

smoothing not only mitigates epitaxial defect formation but also strengthens electronic passivation in SHJ bottom cell, forming the basis for the superior tandem integration. The corresponding implied open-circuit voltage distributions are summarized in Figure S14. The combined structural and lifetime measurements therefore directly correlate the suppression of local partial epitaxial ordering with improved interface passivation after rounding. At a larger length scale, additional cross-sectional TEM (Figure S15) shows that the ITO layer largely follows the underlying textured geometry without planarizing the submicron pyramid profile, while local surface variations remain observable after ITO deposition (Figure S16). This confirms that the morphology presented to the subsequently deposited PVSK stack remains distinct between the irregular and rounded configurations.

1.4 | Formation of Perovskite Film and Tandem Performance

After clarifying the impact of pyramid morphology on the SHJ bottom cells, we examined how the morphological modification affects PVSK film formation and tandem device performance. Here, the top cell employs a typical triple-cation halide perovskite, $Cs_{0.05}(FA_{0.77}MA_{0.23})_{0.95}Pb(I_{0.77}Br_{0.23})_3$ (FA and MA are formamidinium and methylammonium, respectively), with a bandgap of 1.68 eV. Figure 4 summarizes the optical and electrical characteristics of the top cells and monolithic tandem devices fabricated on irregular and rounded submicron textured bottom cells.

To quantitatively evaluate the top cell quality, steady-state photoluminescence (SSPL) was performed on both configurations (Figure S17a). The Fermi-level splitting ΔE_F was derived from the external luminescence quantum yield Q_e^{lum} according to [32]

$$\Delta E_F = k_B T \ln\left(Q_e^{lum} J_G / J_0^{rad}\right) \quad (3)$$

where J_G is the photogenerated current density and J_0^{rad} is the radiative saturation current density. The rounded sample exhibits a higher Q_e^{lum} and a higher ΔE_F of approximately 1.25 V (Figure S17b), indicating lower non-radiative recombination. Spatial ΔE_F maps of the top cells (Figure 4a) show pronounced inhomogeneity for irregular submicron textures, whereas the rounded configuration presents a markedly brighter and more uniform ΔE_F. The corresponding histogram shown in Figure 4b further confirms a narrower distribution, consistent with reduced spatial optoelectronic heterogeneity.

These trends can be rationalized by the smoother, chemically rounded Si pyramids, which reduce both sharp tips and micro-terrace steps. On irregular textures, high-curvature regions and micro-terraces are expected to perturb local wetting and solvent removal during spin–coating, leading to variations in drying dynamics and subsequent film formation [33]. Similar sensitivity

16146840, 0, Downloaded from https://advanced.onlinelibrary.wiley.com/doi/10.1002/aenm.71784 by Universitatsbibliothek RWTH Aachen University, Wiley Online Library on [13/11/2025]. See the Terms and Conditions (https://onlinelibrary.wiley.com/terms-and-conditions) on Wiley Online Library for rules of use; OA articles are governed by the applicable Creative Commons License

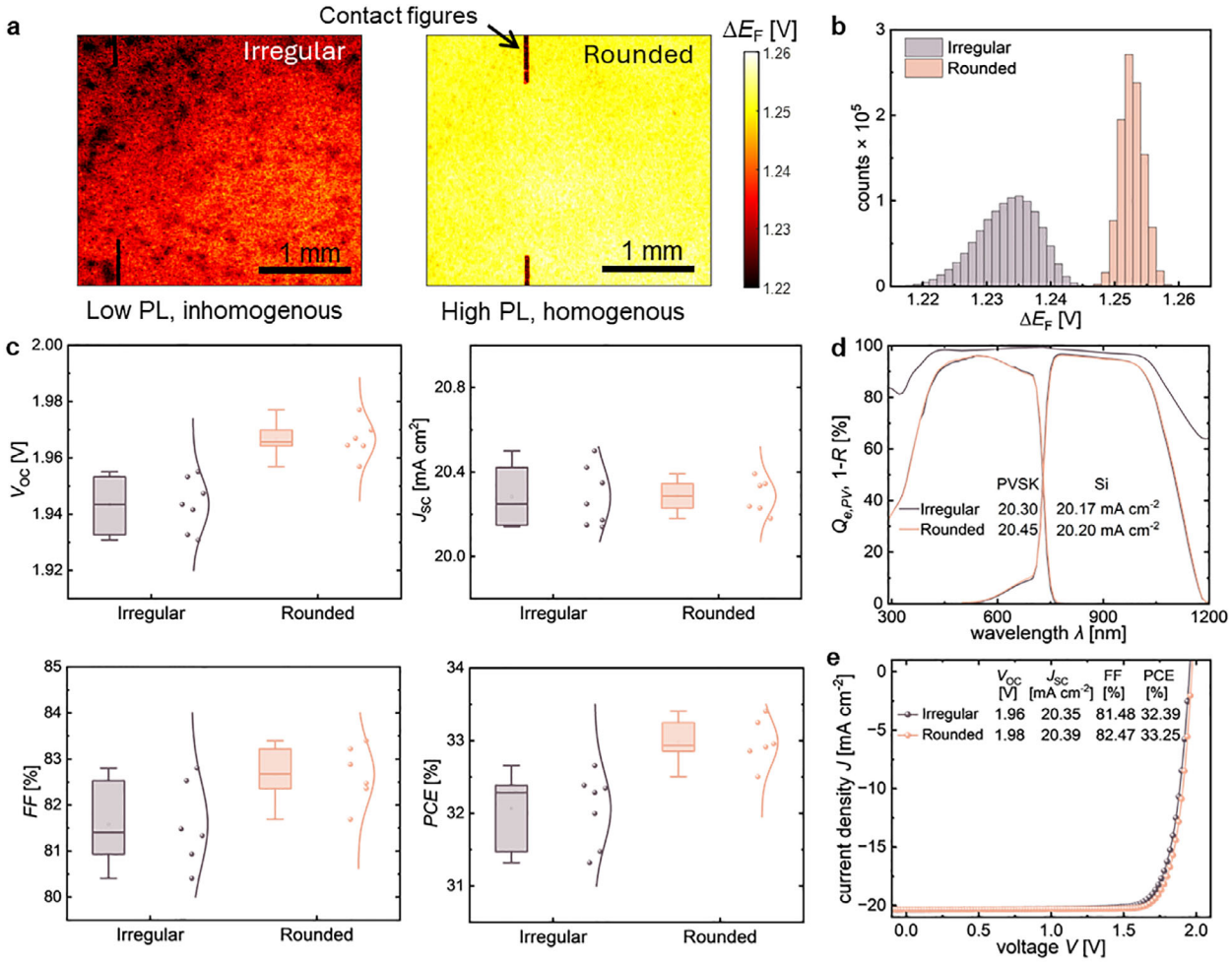

FIGURE 4 | (a) ΔE_F maps and (b) Histogram of ΔE_F of top cell deposited on irregular textured and rounded textured SHJ bottom cell. (c) Statistics of V_{OC}, J_{SC}, FF and efficiency of irregular and rounded textured tandem devices. (d) $Q_{e,PV}$ and 1–R spectra of irregular and rounded-textured tandem devices. (e) J–V curves for irregular and rounded-textured tandem devices.

of perovskite integration to texture morphology has been reported on black silicon, steep micron-scale pyramids and patterned V-groove textures, where rough or sharp features were associated with porous scaffolds, pinholes and dark PL regions, whereas gentler or flattened geometries yielded more uniform films [34–36].

Additional top-view and cross-sectional SEM measurements (Figure S18) were therefore performed to further examine the morphology-dependent film formation. Top-view SEM shows no pronounced difference in the overall perovskite grain morphology between the two configurations, whereas cross-sectional SEM (Figure S18c,d) reveals more frequent localized crack-like discontinuities in the perovskite layers deposited on the irregular texture. In contrast, the rounded texture generally supports a more continuous film morphology. To determine whether these morphological differences are accompanied by substantial changes in the bulk PVSK crystal structure, additional x-ray diffraction (XRD) and grazing-incidence x-ray diffraction (GIXRD) measurements were performed. The diffraction patterns (Figure S19) are highly comparable for the two samples, with no obvious peak shift or differences in peak width and only modest variations in peak intensity. These results therefore do not indicate a pronounced change in bulk PVSK structure.

The enhanced ΔE_F and its improved spatial uniformity are thus more consistently associated with improved film integrity and morphology-dependent buried-interface quality rather than with pronounced changes in bulk perovskite crystallization. In addition, the modified ITO-coated surface morphology may influence the formation of the self-assembled monolayers and thereby contribute to the buried-interface quality.

With all the assessments of the bottom cell and top cell, the tandem device performance summarized in Figure 4c further validates the positive impact of surface rounding. Devices based on rounded textures exhibit an open-circuit voltage (V_{OC}) exceeding 1.96 V, approximately 20 mV higher than that of devices with irregular textures. The same overall trend was reproduced in an independently fabricated device batch (Figure S20). This gain is consistent with the enhancement in ΔE_F of the top cells and the improved a-Si:H/c-Si passivation of the bottom cells. Both configurations present comparable short-circuit current density (J_{SC}) values, indicating that the slight increase in reflectance associated with the rounded tips does not compromise the

16146840, 0, Downloaded from https://advanced.onlinelibrary.wiley.com/doi/10.1002/aenm.71784 by Universitatsbibliothek RWTH Aachen University, Wiley Online Library on [13/11/2025]. See the Terms and Conditions (https://onlinelibrary.wiley.com/terms-and-conditions) on Wiley Online Library for rules of use; OA articles are governed by the applicable Creative Commons License

light-trapping capabilities of the bottom cells (Figure 4d). In addition, the rounded tandem devices exhibit a higher fill factor (*FF*), consistent with reduced morphology-related electrical losses in the integrated device stack. Consequently, the rounded devices achieve a power conversion efficiency (PCE) of 33.25% (Figure 4e). Rather than originating from optical gains alone, this improvement reflects the combined effects of enhanced bottom-cell passivation, reduced non-radiative recombination in top-cell stack, and improved morphology-dependent film and interfacial quality.

2 | Conclusion

In this study, we established a design strategy for the Si bottom cell that enables both efficient light management and high interface quality for tandem integration by using optical simulation to inform processing. Guided by the simulation insights, controlled submicron textures were experimentally realized through precise KOH-based etching, followed by an O_3-assisted chemical rounding treatment that produced smoother and more symmetric pyramid facets. The rounded morphology effectively suppressed epitaxial ordering at the a-Si:H/c-Si interface and improved the passivation quality of the SHJ bottom cell. For subsequent top-cell integration, the rounded texture was associated with improved film integrity and reduced morphology-dependent interfacial losses without inducing a pronounced change in the bulk perovskite crystal structure. As a result, the rounded configuration exhibited higher Q_e^{lum}, a more homogeneous ΔE_F distribution and superior tandem performance with an efficiency of 33.25%. These findings establish a direct link between the bottom cell texture morphology, interfacial microstructure, and tandem device performance, underscoring the critical importance of precise morphological control for highly efficient PST solar cells.

3 | Methods

3.1 | Materials

N, N-Dimethyl formamide (DMF), dimethyl sulfoxide (DMSO), isopropanol (IPA, anhydrous), and ethyl acetate (99.8%) were purchased from Sigma–Aldrich. Ethanol (99.8%, anhydrous) was purchased from VWR Chemicals. Cesium iodide (CsI, 99.999%) and magnesium fluoride (MgF_2, 99.99%) were purchased from Thermo Fisher Scientific Inc. Formamidinium iodide (FAI, 99.99%), methylammonium bromide (MABr, >99.99%) and methylammonium chloride (MACl, 99.99%) were purchased from GreatCell Solar. Lead iodide (PbI_2, 99.99%), lead bromide ($PbBr_2$, 98.0%), lead chloride ($PbCl_2$, >99.0%) and [4-(7H-Dibenzo[c,g]carbazol-7-yl)butyl]phosphonic Acid (4PADCB, >98.0%) were purchased from TCI. Piperazine iodide (PI, 99.5%) was purchased from YuriSolar. Fullerene (C_{60}, 99.5%) was purchased from Ossila Ltd.

3.2 | Fabrication of Si Bottom Cells

SHJ bottom cells were fabricated on the double-side-polished, *n*-type, (100)-oriented, 4-inch float zone (FZ) wafers with the thickness of 280 μm and the resistivity of 1 – 5 Ω · cm. The texturing process was done in a KOH-based solution to obtain randomly distributed pyramids. To further improve the surface wetting and promote hydrogen-bubble detachment effectively, 0.9% texturing additive (HJ21V20) from Scenergy was used. The KOH concentration was adjusted from 0.23%, 0.28% to 0.33%, respectively, to achieve different pyramid heights. The texturing temperature was kept constant at 80°C, and the processing time was 7 min. The rounding treatment was carried out in an isotropic etching solution of HF, HCl, and 20 ppm O_3 for 3 min. The HCl stabilizes the dissolved O_3 against decomposition and removes trace metallic impurities, thereby preventing surface redeposition and ensuring uniform etching. After texturing, a standard O_3 cleaning procedure followed by a native oxide removal process in 1% HF was performed before further thin film depositions. The hydrogenated intrinsic a-Si:H (i) and phosphorus-doped a-Si:H (n) stack was deposited on the front side by a PECVD system, with the thickness of approximately 6 nm. Subsequently, a-Si:H (i) and boron-doped a-Si:H (p) were deposited on the rear side with the thickness of 6 nm and 13 nm, respectively. On the rear side, 70 nm tin-doped indium oxide (ITO) and 1 μm silver were sputtered to achieve good contact through a mask with the aperture area of 1.1×1.1 cm^2. On the front side, 20 nm ITO was deposited as the recombination layer with the aligned mask. To recover sputter damage, a heat-assisted light soaking at 175°C was carried out for 180 s. Finally, the bottom cells were laser-scribed to a size of 2×2 cm^2 for tandem fabrication.

3.3 | Fabrication of Perovskite Top Cells

The bottom cells were oxygen-plasma treated for 12 min. Then, the samples were rapidly transferred into a nitrogen-filled glovebox for further deposition. For the hole transport layer, 90 μL 4PADCB (1 mg/mL in ethanol) was spin–coated at 3000 rpm for 30 s, followed by an annealing step on a hot plate at 100°C for 10 min. 1.7 M wide-bandgap perovskite precursor solution with the composition of $Cs_{0.05}(FA_{0.77}\ MA_{0.23})_{0.95}Pb(I_{0.77}Br_{0.23})_3$ and 3% excess $MAPbCl_3$ was prepared by dissolving 22.1 mg CsI, 41.6 mg MABr, 213.9 mg FAI, 147.1 mg $PbBr_2$, 599 mg PbI_2 in 1 mL mixed solvent of DMF and DMSO (v:v = 4:1). The precursor solution was filtered with a 0.45 μm PTFE filter before use. 100 μL precursor solution was first spin–coated at 1000 rpm for 7 s, subsequently at 3000 rpm for the last 25 s. 300 μL of anti-solvent ethyl acetate (EA) was dropped on the substrate at 10 s before the end of spinning. Then the film was annealed at 100°C for 15 min. For the passivation layer, 90 μL PI (0.2 mg/mL in IPA) was dynamically spin–coated on the perovskite film at 5000 rpm for 30 s, followed by the thermal annealing at 100°C for 10 min. Then, 10 nm C_{60} was thermally evaporated at 0.2 Å s^{-1}.

Afterward, the samples were transferred to an ALD system (TFS200, Beneq). 100 cycles of SnO_x (~15 nm) were deposited at 80°C. Tetrakis(dimethylamino)tin(IV) (TDMASn) and deionized water were used as tin and oxygen precursors. During deposition, the TDMASn precursor was maintained at 55°C and water was kept at room temperature. Nitrogen was used as the carrier gas with flow rate of 500 sccm, purging the inner chamber continuously. One cycle of the ALD process consists of the following sequence: TDMASn pulse (1 s)/N_2 purge (30 s)/deionized water (1 s)/N_2 purge (30 s). A 40 nm Zinc-doped indium oxide (IZO) film was deposited on top of SnO_x by

16146840, 0, Downloaded from https://advanced.onlinelibrary.wiley.com/doi/10.1002/aenm.71784 by Universitatsbibliothek RWTH Aachen University, Wiley Online Library on [13/11/2025]. See the Terms and Conditions (https://onlinelibrary.wiley.com/terms-and-conditions) on Wiley Online Library for rules of use; OA articles are governed by the applicable Creative Commons License

radio-frequency magnetron sputtering through a patterned mask. Later, 500 nm silver was evaporated on top of IZO with a precisely aligned mask (device area 1.014 cm^2). Finally, 100 nm MgF_2 was evaporated as anti-reflection coating.

3.4 | Characterizations

The effective minority carrier lifetime was investigated by quasi-steady-state photoconductance (Sinton WCT-120) with the transient mode. The iV_{OC} was extracted at $\Delta n = 5 \times 10^{15}$ cm^{-3}. The surface morphology and cross-sectional images were characterized by scanning electron microscopy (FESEM ZEISS LEO 1550 VP). The cross-sectional TEM samples for atomic-resolution STEM images were fabricated by the Tescan Solaris Focused Ion Beam (FIB) dual-beam system. The STEM images were obtained using an aberration-corrected JEOL ARM300F2 operated at 300 kV. The convergence semi-angle was 24.9 mrad, the angular range of the ADF detector was from 45 to 180 mrad and the angular range of the bright field detector was from 0 to 30 mrad. Image processing was performed in DigitalMicrograph (Gatan). The reflectance of wafers and devices was measured by the LOANA system from PV-Tools. The XRD measurements were performed using a Rigaku SmartLab diffractometer in a coupled θ–2θ configuration. The diffraction patterns were recorded over a 2θ range of 5°–60° with a step size of 0.02°. GIXRD measurements were performed using the same instrument at a fixed grazing-incidence angle of 0.9°. The measured intensity was expressed in counts per second (cps). The SSPL spectra and quantum yield of the film stacks were measured by the setup from QY.Berlin with the excitation laser wavelength of 532 nm and a spot size of 1 cm^2. The laser intensity was set to 1 sun. The *J*–*V* curves were performed with a Keithley 2450 device under a calibrated AM1.5G spectrum from a light-emitting diode solar simulator (Wavelabs SINUS-70 ADVANCED) integrated underneath N_2-filled glovebox. The intensity was calibrated to 100 mW/cm^2 by a monocrystalline silicon reference cell (Oriel 91150 V), certified by Newport Corporation's PV Lab (North Logan, UT). The *J*–*V* curves were scanned from 2 to −0.1 V with a step of 0.02 V. The external quantum efficiency of the tandem device was measured in ambient air with the LOANA system. When measuring the bottom subcell, 1.1 V bias voltage and blue bias light of 450 nm with 6.6 mW/cm^2 intensity were applied on the device, while 0.7 V bias voltage and infrared bias light from a halogen lamp by RG 830 filter with 11.4 mW/cm^2 intensity were applied on the device when measuring the top subcell. The photoluminescence images were acquired with an in-house-built setup in ambient air. The samples were illuminated by a 470 nm blue laser, and the background was measured for flat-field correction. Data acquisition was accomplished with an exposure time of 0.8 s and three accumulations. The film thickness and optical properties were determined by a spectroscopic ellipsometer (J.A. Woollam M-2000).

Author Contributions

N.S. and K.D. conceived the idea and designed the experiments. B.X. and K.B. developed the optical simulation for tandem architecture. N.S. developed the texture process and optimized the tandem device. G.H. developed the perovskite top cell fabrication process. Y.L. and E.N. performed the STEM and SEM measurement respectively. A.L. fabricated the SHJ bottom cells. All authors provided feedback and comments for the manuscript revision.

Acknowledgements

This work was supported by the project "Zeitenwende–Zukunftstechnologie Tandem–Solarzellen" funded by the HGF (Helmholtz association) and the project "SuperSolid" funded under the grant number 03EE1181B by the Federal Ministry for Economic Affairs and Climate Action on the basis of a decision by the German Bundestag. N.S. acknowledges the support from China Scholarship Council (No. 202206290060).

Open access funding enabled and organized by Projekt DEAL.

Conflicts of Interest

The authors declare no conflicts of interest.

Data Availability Statement

The data that support the findings of this study are available in the supplementary material of this article.

References

1. Z. Hameiri, "Photovoltaics Literature Survey (No. 180)," *Progress in Photovoltaics: Research and Applications* 31 (2023): 195–199, https://doi.org/10.1002/pip.3662.

2. D. C. Jordan and S. R. Kurtz, "Photovoltaic Degradation Rates—an Analytical Review," *Progress in Photovoltaics: Research and Applications* 21 (2013): 12–29, https://doi.org/10.1002/pip.1182.

3. T. Niewelt, B. Steinhauser, A. Richter, et al., "Reassessment of the Intrinsic Bulk Recombination in Crystalline Silicon," *Solar Energy Materials and Solar Cells* 235 (2022): 111467, https://doi.org/10.1016/j.solmat.2021.111467.

4. M. A. Green, E. D. Dunlop, M. Yoshita, et al., "Solar Cell Efficiency Tables: Version 68," *Joule* 10 (2026): 102494, https://doi.org/10.1016/j.joule.2026.102494.

5. C. Kan, P. Hang, S. Wang, et al., "Efficient and Stable Perovskite-silicon Tandem Solar Cells With Copper Thiocyanate-embedded Perovskite on Textured Silicon," *Nature Photonics* 19 (2025): 63–70, https://doi.org/10.1038/s41566-024-01561-5.

6. Z. Liu, S. Yang, Y. Tian, et al., "Homogeneity Regulation in Sequential Fabricated Perovskite Film for Industrial-Scale Deposition of Fully-Textured Perovskite/Silicon Tandem Cells," *Advanced Materials* 38 (2026): e11177, https://doi.org/10.1002/adma.202511177.

7. A. Al-Ashouri, E. Köhnen, B. Li, et al., "Monolithic Perovskite/Silicon Tandem Solar Cell With >29% Efficiency By Enhanced Hole Extraction," *Science* 370 (2020): 1300–1309, https://doi.org/10.1126/science.abd4016.

8. F. J. Haug and C. Ballif, "Light Management in Thin Film Silicon Solar Cells," *Energy & Environmental Science* 8 (2015): 824–837, https://doi.org/10.1039/C4EE03346A.

9. M. K. Basher, M. K. Hossain, M. J. Uddin, M. A. R. Akand, and K. M. Shorowordi, "Effect of Pyramidal Texturization on the Optical Surface Reflectance of Monocrystalline Photovoltaic Silicon Wafers," *Optik* 172 (2018): 801–811, https://doi.org/10.1016/j.ijleo.2018.07.116.

10. J. Wang, F. Zhong, H. Liu, et al., "Influence of the Textured Pyramid Size on the Performance of Silicon Heterojunction Solar Cell," *Solar Energy* 221 (2021): 114–119, https://doi.org/10.1016/j.solener.2021.04.021.

11. S. Xia, F. Wang, P. Chen, et al., "Advanced Sub-Micron Pyramid Texture Enables Approximately 32% Efficiency in Perovskite/Silicon Tandem Solar Cells," *Advanced Functional Materials* 36 (2026): 25903, https://doi.org/10.1002/adfm.202525903.

16146840, 0, Downloaded from https://advanced.onlinelibrary.wiley.com/doi/10.1002/aenm.71784 by Universitatsbibliothek RWTH Aachen University, Wiley Online Library on [13/11/2025]. See the Terms and Conditions (https://onlinelibrary.wiley.com/terms-and-conditions) on Wiley Online Library for rules of use; OA articles are governed by the applicable Creative Commons License

12. M. Gosálvez, K. Sato, A. Foster, R. Nieminen, and H. Tanaka, "An Atomistic Introduction to Anisotropic Etching," *Journal of Micromechanics and Microengineering* 17 (2007): S1–S26, https://doi.org/10.1088/0960-1317/17/4/S01.

13. A. Moldovan, T. Dannenberg, J. Temmler, L. Kroely, M. Zimmer, and J. Rentsch, "Ozone-based Surface Conditioning Focused on an Improved Passivation for Silicon Heterojunction Solar Cells," *Energy Procedia* 92 (2016): 374–380, https://doi.org/10.1016/j.egypro.2016.07.115.

14. Y. Hou, E. Aydin, M. De Bastiani, et al., "Efficient Tandem Solar Cells With Solution-processed Perovskite on Textured Crystalline Silicon," *Science* 367 (2020): 1135–1140, https://doi.org/10.1126/science.aaz3691.

15. J. Zheng, C. F. J. Lau, H. Mehrvarz, et al., "Large Area Efficient Interface Layer Free Monolithic Perovskite/Homo-junction-silicon Tandem Solar Cell With Over 20% Efficiency," *Energy & Environmental Science* 11 (2018): 2432–2443, https://doi.org/10.1039/C8EE00689J.

16. J. Liu, Y. He, L. Ding, et al., "Perovskite/Silicon Tandem Solar Cells With Bilayer Interface Passivation," *Nature* 635 (2024): 596–603, https://doi.org/10.1038/s41586-024-07997-7.

17. T. Kirchartz, A. Helbig, W. Reetz, M. Reuter, J. H. Werner, and U. Rau, "Reciprocity Between Electroluminescence and Quantum Efficiency Used for the Characterization of Silicon Solar Cells," *Progress in Photovoltaics: Research and Applications* 17 (2009): 394–402, https://doi.org/10.1002/pip.895.

18. N.-G. Park, "Perovskite Solar Cells: An Emerging Photovoltaic Technology," *Materials Today* 18 (2015): 65–72, https://doi.org/10.1016/j.mattod.2014.07.007.

19. H. T. Gebrewold, K. Bittkau, K. Qiu, U. Rau, and K. Ding, "Understanding Silicon Heterojunction Solar Cells With nc-SiC/SiO_2 as an Alternate Transparent Passivating Front Contact and Computational Design Optimization," *Solar RRL* 7 (2023): 2201051, https://doi.org/10.1002/solr.202201051.

20. U. Chime, L. Wolf, V. Buga, et al., "How Thin Practical Silicon Heterojunction Solar Cells Could Be? Experimental Study Under 1 Sun and Under Indoor Illumination," *Solar RRL* 6 (2022): 2100594, https://doi.org/10.1002/solr.202100594.

21. B. Xu, A. Eberst, P. Fall, et al., "Restoring Sputter Damage by Light Soaking in Silicon Carbide-based Transparent Passivating Contact Solar Cells," *Cell Reports Physical Science* 6 (2025): 102552, https://doi.org/10.1016/j.xcrp.2025.102552.

22. C. Battaglia, A. Cuevas, and S. De Wolf, "High-efficiency Crystalline Silicon Solar Cells: Status and Perspectives," *Energy & Environmental Science* 9 (2016): 1552–1576, https://doi.org/10.1039/C5EE03380B.

23. M. De Bastiani, et al., "Monolithic Perovskite/Silicon Tandems With >28% Efficiency: Role of Silicon-Surface Texture on Perovskite Properties," *Advanced Functional Materials* 33 (2023): 2205557, https://doi.org/10.1002/adfm.202205557.

24. Y. Li, H. Sai, C. McDonald, et al., "Nanoscale Size Control of Si Pyramid Texture for Perovskite/Si Tandem Solar Cells Enabling Solution-Based Perovskite Top-Cell Fabrication and Improved Si Bottom-Cell Response," *Advanced Materials Interfaces* 10 (2023): 2300504, https://doi.org/10.1002/admi.202300504.

25. A. Alasfour, Z. J. Yu, W. Weigand, D. Quispe, and Z. C. Holman, "Sub-Micrometer Random-pyramid Texturing of Silicon Solar Wafers With Excellent Surface Passivation and Low Reflectance," *Solar Energy Materials and Solar Cells* 218 (2020): 110761, https://doi.org/10.1016/j.solmat.2020.110761.

26. H. Sai, Y. Kanamori, K. Arafune, Y. Ohshita, and M. Yamaguchi, "Light Trapping Effect of Submicron Surface Textures in Crystalline Si Solar Cells," *Progress in Photovoltaics: Research and Applications* 15 (2007): 415–423, https://doi.org/10.1002/pip.754.

27. P. Pal, V. Swarnalatha, A. V. N. Rao, A. K. Pandey, H. Tanaka, and K. Sato, "High Speed Silicon Wet Anisotropic Etching for Applications in Bulk Micromachining: A Review," *Micro and Nano Systems Letters* 9 (2021): 4, https://doi.org/10.1186/s40486-021-00129-0.

28. K. Singh, M. Nayak, S. Mudgal, S. Singh, and V. K. Komarala, "Effect of Textured Silicon Pyramids Size and Chemical Polishing on the Performance of Carrier-selective Contact Heterojunction Solar Cells," *Solar Energy* 183 (2019): 469–475, https://doi.org/10.1016/j.solener.2019.03.059.

29. J. Du, F. Meng, H. Fu, et al., "Selective Rounding for Pyramid Peaks and Valleys Improves the Performance of SHJ Solar Cells," *Energy Science & Engineering* 9 (2021): 1306–1312, https://doi.org/10.1002/ese3.900.

30. H. Zhang, K. Nakada, and M. Konagai, "Effects of Epitaxial Growth on the Optimum Condition of Intrinsic Amorphous Silicon Oxide Buffer Layers for Silicon Heterojunction Solar Cells," *Thin Solid Films* 628 (2017): 214–220, https://doi.org/10.1016/j.tsf.2017.03.040.

31. J.-H. An, J.-E. Hong, J.-H. Oh, S. H. Kong, and K.-H. Kim, "Suppression of Parasitic Epitaxy Growth and Realization of High-Quality Wafer Surface Passivation of Silicon Heterojunction Solar Cells," *Journal of the Korean Physical Society* 76 (2020): 442–446, https://doi.org/10.3938/jkps.76.442.

32. P. Caprioglio, M. Stolterfoht, C. M. Wolff, et al., "On the Relation Between the Open-Circuit Voltage and Quasi-Fermi Level Splitting in Efficient Perovskite Solar Cells," *Advanced Energy Materials* 9 (2019): 1901631, https://doi.org/10.1002/aenm.201901631.

33. G. Zhang, B. Ding, Y. Ding, et al., "Suppressing Interfacial Nucleation Competition Through Supersaturation Regulation for Enhanced Perovskite Film Quality and Scalability," *Science Advances* 10 (2024): adl6398, https://doi.org/10.1126/sciadv.adl6398.

34. S.-W. Lee, S. Bae, J.-K. Hwang, et al., "Perovskites Fabricated on Textured Silicon Surfaces for Tandem Solar Cells," *Communications Chemistry* 3 (2020): 37, https://doi.org/10.1038/s42004-020-0283-4.

35. E. M. Tennyson, K. Frohna, W. K. Drake, et al., "Multimodal Microscale Imaging of Textured Perovskite–Silicon Tandem Solar Cells," *ACS Energy Letters* 6 (2021): 2293–2304, https://doi.org/10.1021/acsenergylett.1c00568.

36. O. Er-raji, A. J. Bett, S. Lange, et al., "Toward Efficient and Industrially Compatible Fully Textured Perovskite Silicon Tandem Solar Cells: Controlled Process Parameters for Reliable Perovskite formation," *Progress in Photovoltaics: Research and Applications* 33 (2025): 86–99, https://doi.org/10.1002/pip.3770.

Supporting Information

Additional supporting information can be found online in the Supporting Information section.

Supporting File: aenm71784-sup-0001-SuppMat.docx.

16146840, 0, Downloaded from https://advanced.onlinelibrary.wiley.com/doi/10.1002/aenm.71784 by Universitatsbibliothek RWTH Aachen University, Wiley Online Library on [13/11/2025]. See the Terms and Conditions (https://onlinelibrary.wiley.com/terms-and-conditions) on Wiley Online Library for rules of use; OA articles are governed by the applicable Creative Commons License